Nuclear Materials and Energy 38 (2024) 101619

Contents lists available at ScienceDirect

Nuclear Materials and Energy

journal homepage: www.elsevier.com/locate/nme

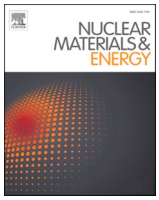

Effect of metal impurities on the adsorption energy of cesium and work function of the cesiated Mo (0 0 1) surface

Heng Li [a], Xin Zhang [a,*], Yuhong Xu [a,*], Guangjiu Lei [b], Sanqiu Liu [c], Katsuyoshi Tsumori [d], Haruhisa Nakano [d], Masaki Osakabe [d], Mitsutaka Isobe [d], Shoichi Okamura [d], Akihiro Shimizu [d], Kunihiro Ogawa [d], Hiromi Takahashi [d], Zilin Cui [a], Jun Hu [a], Yiqin Zhu [a], Xiaolong Li [a], Huaqing Zheng [a], Xiaoqiao Liu [a], Shaofei Geng [b], Xiaochang Chen [c], Haifeng Liu [a], Xianqu Wang [a], Hai Liu [a], Changjian Tang [a,e], CFQS team[a,d]

[a] Institute of Fusion Science, School of Physical Science and Technology, Southwest Jiaotong University, Chengdu 610041, China
[b] Southwestern Institute of Physics, Chengdu 610041, China
[c] Jiangxi Province Key Laboratory of Fusion and Information Control, Department of Physics, Nanchang University, Nanchang 330031, China
[d] National Institute for Fusion Science, National Institutes of Natural Science, Toki 5095259, Japan
[e] School of Physical Science and Technology, Sichuan University, Chengdu 610041, China

ARTICLE INFO

Keywords:
DFT
Work function
Negative ion source
Cesiated surface
Metal impurities
Dipole moment

ABSTRACT

Based on the DFT method, the effects of copper and tungsten impurities present in the negative ion source of neutral beams on the cesiated surface were studied, including their effects on the adsorption energy of cesium on the surface and the surface work function. The results indicate that copper impurities significantly increase the average adsorption energy of cesium, whereas tungsten has limited enhancement on the average adsorption energy of cesium and may even reduce it. The work function calculations show that, at cesium coverages below 4/16 θ, copper impurities cause a significant increase in the work function. However, at cesium coverages above 6/16 θ, high-coverage copper impurities lead to a further decrease in the work function, causing the cesium coverage corresponding to the lowest work function to shift towards higher cesium coverage. Under any tungsten impurity and cesium coverage, tungsten impurities can significantly increase the surface work function, with the maximum increase reaching 0.50 eV. The dipole moment density analysis shows that in most cases, impurities significantly reduce the dipole moment density of the cesiated surface, except when the coverage of cesium and copper impurities is above 6/16 θ. The charge transfer results show that the copper impurity layer has more positive charge compared to the tungsten impurity layer, which significantly affects the dipole moment density of the surface system. In addition, adsorbed atoms cause electrons in the molybdenum atomic layer to migrate to the surface, resulting in the molybdenum substrate having a pronounced negative dipole moment.

1. Introduction

The NBI system is one of the most effective methods for heating magnetically confined plasma and driving plasma current. There are two NBI types: negative ion-based (NNBI) and positive ion-based (PNBI). Their key distinction is their acceleration tactics: NNBI accelerates negative hydrogen ions, while PNBI accelerates positive ones. Regardless of ion type, after acceleration, they're neutralized, hence called "neutral beams." Positive ions' neutralization efficiency is minimal at high energy, making them unsuitable for 1 MeV targets in ITER [1]. Conversely, negative ions have about 60 % efficiency under similar conditions [2]. In both radio frequency (RF) and tungsten filament sources, initial plasma contains few negative ions. Most are later generated in volume and surface processes, with the latter being predominant [3]. These negative ions form on the plasma grid (PG), typically molybdenum-made, with a porous design crucial for ion extraction. The PG surface, termed the converter surface, witnesses cesium deposition and negative ion creation. It also acts as an electrode in a series-connected accelerator, which may vary across facilities [4–11]. Negative ions form on the PG surface, migrate to the extraction region,

* Corresponding authors.
E-mail addresses: xzhang@my.swjtu.edu.cn (X. Zhang), xuyuhong@swjtu.edu.cn (Y. Xu).

https://doi.org/10.1016/j.nme.2024.101619
Received 23 November 2023; Received in revised form 5 February 2024; Accepted 18 February 2024
Available online 20 February 2024

and are curved by the extraction field before exiting via PG apertures [12]. The production efficiency of negative hydrogen ions is related to the work function of the PG surface. Taking molybdenum metal as an example, its work function is typically greater than 4 eV [13]. To effectively reduce the work function of the PG surface, depositing cesium atoms on the PG surface is currently the most common practice. Molybdenum metal surfaces with 0.5 ML Cs coverages can have work functions below 1.8 eV [14–17].

The interior of the negative ion source is a complex environment. In addition to cesium vapor atoms, there are plasmas, gaseous hydrogen molecules, and trace amounts of oxygen and water vapor, among other impurities [18–23]. Impurities, including plasma particles, have a significant impact on the work function of cesiated surfaces. Experimental work by Papageorgopoulos et al. [15,16] demonstrated the significant impact of non-metal impurities such as oxygen and hydrogen on the work function of cesiated surfaces. They believed that at a sub-monolayer cesium coverage, non-metal impurities can further reduce the surface work function. However, at one monolayer cesium coverage, these impurities tend to increase the surface work function.

In our previous theoretical work [24], we reproduced the experimental results reported by Papageorgopoulos et al. We believe that cesium and co-deposited non-metal impurities form a double layer structure on the surface. This double layer consists of an electropositive layer (cesium) and an electronegative layer (impurities). Such a structure has a strong intrinsic dipole moment, which can greatly reduce the surface work function. However, due to the strong electronegativity of the impurity layer, it can effectively attract electrons from the substrate atoms, forming an opposite dipole moment, which in turn can significantly increase the surface work function. The competition between these two effects leads to a uncertainty in the change of the surface work function. Besides, there are many specific reports studying the effects of non-metal impurities like hydrogen and oxygen on the work function of cesiated surfaces. Said et al. [21] investigated the impact of low-coverage non-metal impurities on the work function of cesiated surfaces and the adsorption energy of cesium, using a method based on configuration space random search. Abraham et al. [25] studied the impact of H on the adsorption energy of cesium on surfaces. Palma et al. [20] studied the effects of oxygen molecules on cesiated surfaces based on the DFT method, suggesting that the surface would form superoxide-like CsO_2.

Most reports primarily focus on non-metal impurities such as oxygen and hydrogen. This is because these non-metal impurities have strong electronegativity, contrasting with cesium. The latter has pronounced electropositivity and often plays the role of losing electrons when interacting with surface atoms, while the former typically acts as an electron acceptor. In the NBI based on negative ion sources, a certain amount of positive ions will inevitably be generated downstream of the accelerator due to collisions between high-energy negative ions and neutral gas. Influenced by the accelerating electric field, these positive ions are accelerated back into the negative ion source. Backstreaming ions can lead to thermal deposition and material sputtering on the backplate of the ion source [22]. In RF ion sources, copper is a typical example of the specific metal impurities present. Copper is the primary material for the Faraday shield, a key component in RF sources. The installation of the Faraday shield is to protect the alumina insulator from erosion by the plasma [11,26]. When the Faraday shield is bombarded by high-energy positive ions, a large amount of copper sputtering can occur, leading to the co-deposition of copper and cesium on the surface [22,27–29]. Some people believe that copper impurities will contaminate the cesiated surface, reducing the performance of the ion source. Moreover, they think that copper and oxygen will chemically react with the cesium layer. To reduce the source of copper impurities, a thin layer of molybdenum was coated on the copper surface of the Faraday shield. The experiment showed that this indeed reduced the amount of copper impurities in the plasma. However, it also proved that the Faraday shield is not the only source of copper impurities. Another source of copper impurities is the cone, which is used to separate the driver region from the expansion region [22]. Bandyopadhyay et al. [30] confirmed the presence of copper spectral lines in the RF ion source using the diagnostic method of Optical Emission Spectroscopy. In filament-arc source, due to the consumption and evaporation of the filament, metal impurities are introduced, which depend on the material of the filament. Inoue et al [31]. have reported on the effects of different filament materials on the volume negative ion sources. They primarily conducted comparative experiments between tungsten filament and tantalum filament, indicating that the yield of H^- from the tungsten filament source is significantly lower, while the co-extracted electron current is higher [3,31]. Inoue et al. obtained some evidence that the filament material affects H^- production via the fresh film deposited on the source wall chamber. In LHD-NBI, Takeiri et al. have reported that after 10,000 shots of discharge, the tungsten filament lost about 2 g of mass. They also believe that in the filament-arc source, tungsten vapor will act as a primary contaminant, reducing the effect of cesium [27,32].

In this work, we primarily studied the effects of metal impurities (copper and tungsten) on cesiated surfaces using the DFT (Density Functional Theory) method.There are few studies on the influence of metal impurities on the surface work function of cesiated surfaces. In order to comprehensively understand the effects of co-deposition of cesium and metal impurities on surface properties at different coverages ($\leq$8/16 θ, 1ML), we constructed 53 different surface systems (Among them, 48 surface structures were constructed for the purposes of this study, while the remaining five surfaces, including the clean Mo(001) surface and the pure cesium-covered Mo(001) surface, were obtained from our previous work [24]). These surface systems include Mo (001) substrates, cesium, and metal impurities. Due to the deposition of only two different types of atoms on the surface, the layering structure of cesium and metal impurities in the vacuum direction is distinct, and it is assumed that cesium and metal impurities are uniformly distributed on the surface. Combined with the fact that different types of atoms have different most stable adsorption sites on the Mo (100) surface, the complexity of the initial structure can be greatly simplified. In this work, we constructed a corresponding high-symmetry surface structure for each different coverage. This work did not consider the co-adsorption of hydrogen isotopes because the introduction of hydrogen would greatly increase the complexity of the surface system, requiring more surface structures (including high-symmetry and random distribution structures) for the same coverage. This makes it difficult to consider adsorbates of different coverages. Therefore, this work study the influence of metal impurities on cesiated surfaces starting from simple high-symmetry models under different coverages, aiming to understand the charge transfer and polarization of the bilayer structure formed by the metal impurity layer and the cesium layer. Since hydrogen isotopes have not been introduced, the scenarios considered in this work do not reflect the true conditions of the PG surface of negative ion sources. The purpose of this work is to study the influence of impurities on the cesiation surface work function under different coverage. Subsequent work will introduce hydrogen isotopes at some representative coverages and construct several high-symmetry and random distribution models for different coverages [21]. For the co-deposition of multi-layer cesium and impurities, AIMD simulations under finite temperature conditions were considered [33]. The details of these surface structures are discussed in Section 2. The paper is organized as follows: Section 2 presents the computation details and surface structures, Section 3 presents computation results and disscutions, and finally Section 4 concludes with the most important findings.

2. Methodology

2.1. Electronic structure calculations

The Vienna ab-initio simulation package (VASP) [34,35] and CP2K software package [36] based on periodic density functional theory

(DFT) were used to perform the calculations. The functions of the two codes are as follows: CP2K is mainly used for relaxation calculations of the initial structure, while VASP further performs relaxation and energy calculations after CP2K. For VASP, the ionic core was described using the projector augmented wave (PAW) method [37] with a plane wave cutoff energy of 650 eV. The total energies and forces converged within 10^{-7} eV/cell and 0.01 eV/Å, respectively. The GGA-PBE [38] functional was used for energy calculations, while the LDA [39] functional was used for work function calculations. For the 2D adsorption system, the DFT-D3 correction [40] and dipole correction [41] scheme were applied. For CP2K, the electronic structure was described using GGA-PBE functional within the Gaussian and plane waves framework. Molecular orbitals of the valence electrons were expanded into TZVP-MOLOPT-SR-GTH basis sets [42], while the atomic core electrons were described through Goedecker-Teter-Hutter (GTH) pseudopotentials [43,44] with a cutoff energy of 400 Ry. The atomic positions were fully relaxed under two convergence criteria: (1) the maximum force component of the current configuration is 4.5×10^{-5} Hartree $Bohr^{-1}$ and (2) the root mean square (RMS) force of the current configuration is 3×10^{-5} Hartree $Bohr^{-1}$. The periodicity was applied in the XY-plane. Monkhorst-Pack scheme [45] with k-points of $4 \times 4 \times 1$ were adopted by all VASP and CP2K calculations.

2.2. Surface structure models

In this work, we are dedicated to studying the impact on the work function under different coverages of metal impurities and cesium. The most potential substrate material for the PG electrode is Mo metal, a substrate of dimension 12.53 Å × 12.53 Å × 6.18 Å (4 lattices × 4 lattices in XY plane, and 5layers in Z axis) was constructed. The bottom two layers of Mo atoms were fixed during the relaxation. A > 20 Å vacuum layer was utilized for all calculations. Five different coverages were used for both impurities and cesium, 0, 2/16 θ, 4/16 θ, 6/16 θ, and 8/16 θ, respectively.The coverage 1 θ corresponds to 1 adatom per Mo surface atom ($1\theta = 1.0 \times 10^{15}$ cm^{-2}).

For a single adsorbed atom, either Cs, Cu, or W atom, there is a most stable site on this 4 × 4 plane. The most stable sites for Cs, Cu, and W are the bridge site, hollow site, and top site, respectively. For atom adsorption with different coverages, the corresponding uniform and highly symmetrical initial structures were constructed, as shown in Fig. 1. For Cs co-deposition with Cu or W impurity, two kinds of initial structures were considered. The one is Cs atoms and impurity atoms adjacent to each other with four different coverages, where the Cs-Cu (or W) bonds lean towards the surface; the other one is Cs atoms and impurity atoms have the same initial XY coordinates, that is the Cs-Cu (or W) bonds perpendicular towards the surface, one implication is that the Cs and impurity coverage is the same in this case, as shown in Fig. 1. For comparison convenience, the initial structures of copper and tungsten deposition are identical. Under the condition of bond tilt, after relaxation, the majority of cesium atoms migrate to hollow positions. While under normal conditions, only coverages of 2/16 θ, 4/16 θ, and 8/16 θ maintain their normal states after relaxation

3. Results and discussion

3.1. Average adsorption energy of cesium

If the cesium atoms can adsorb on the PG electrode surface stably is an important issue for Cs consumption and maintaining of the negative ion source. The calculation of the average adsorption energy of cesium is as follows:

$$E_{ad} = (E_{total} - E_{sub} - nE_{Cs})/n$$
$$= [(E_{total} - E'_{sub} - E_{Cs-layer})$$
$$+ (E'_{sub} - E_{sub}) + (E_{Cs-layer} - nE_{Cs})]/n$$
$$= (\Delta E_1 + \Delta E_2 + \Delta E_3)/n\# \quad (1)$$

where E_{total} is the total energy of the surface covered by adatom. E_{sub} is the energy of the substrate (including impurity-covered substrate). E_{Cs} is the energy of the Cs atom in the gas phase. E'_{sub} and $E_{Cs-layer}$ represent the total energies of the deformed substrates and the free-standing Cs layer, respectively. Therefore, ΔE_1 represents the binding energy of the Cs layer on the deformed substrates, ΔE_2 represents the energy required for surface deformation, and ΔE_3 represents the formation energy of n Cs atoms from the isolated gas phase to a Cs layer. For convenience, the energies discussed below correspond to their absolute values (unless stated otherwise).

The results of the adsorption energy of Cs co-deposition with Cu and W are shown in Fig. 2. When the coverage of Cs is certain, the average adsorption energy increases with the increase of Cu coverage. Compared to the pure Cs deposition, the average adsorption energy of Cs co-depositing with 8/16 θ Cu can increase by 0.77 eV for 2/16 θ Cs coverage, by 0.68 eV for 4/16 θ Cs coverage, by 0.61 eV for 6/16 θ Cs

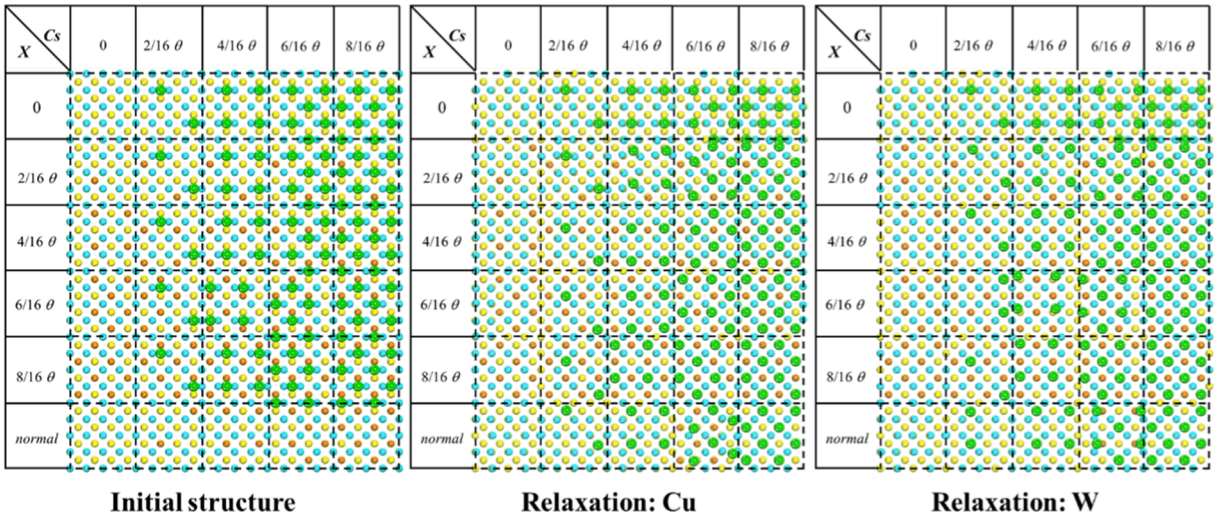

Fig. 1. Initial and relaxation surface structures of adatoms cover on Mo (0 0 1) surface, including pure Cs and pure impurity (X represents Cu or W) adsorption, and Cs co-deposition with impurity atoms. The coverage increases from 0 to 8/16 θ. Green represents cesium atoms, brown represents impurity atoms, blue represents the first layer of molybdenum atoms, and yellow represents the second layer of molybdenum atoms."Normal" denotes the overlapping projection of cesium atoms and impurity atoms on the plane, with impurity atoms being obstructed due to the larger volume of cesium atoms.

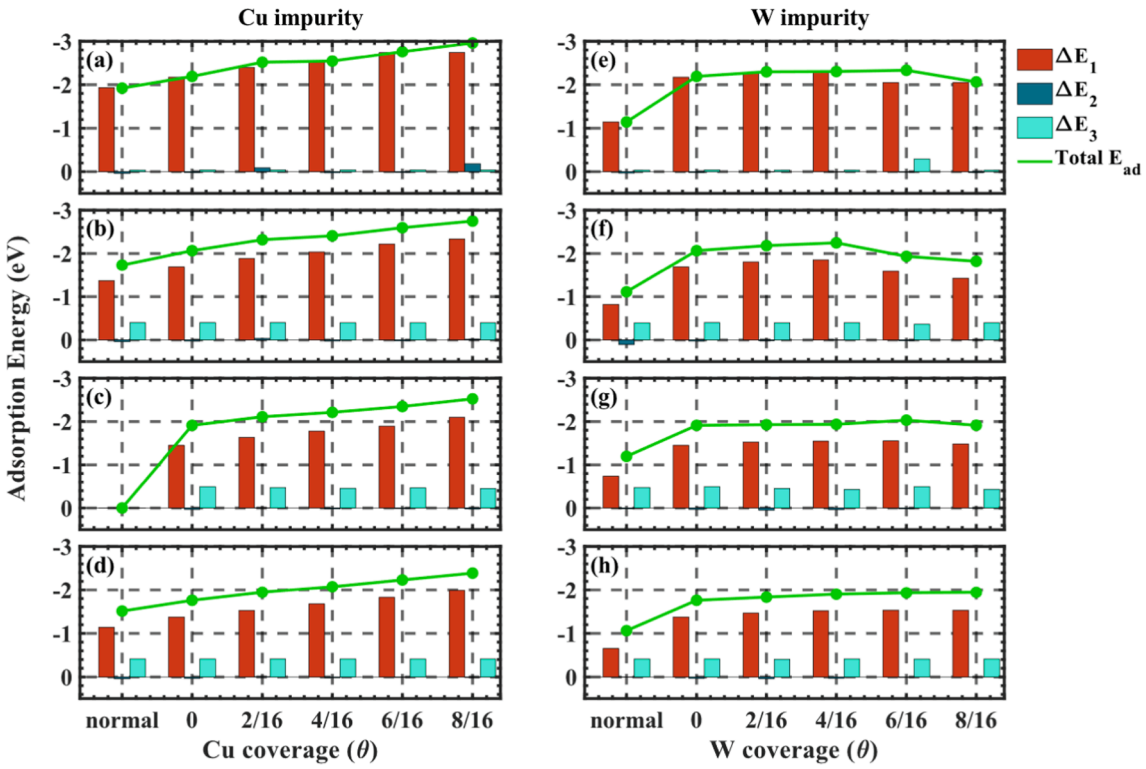

Fig. 2. Adsorption energy of Cs atoms: (a)-(d) for Cs atoms co-deposition with Cu atoms with different Cs coverages, 2/16 θ, 4/16 θ, 6/16 θ, and 8/16 θ, respectively; (e)-(h) for Cs atoms co-deposition with W atoms with different Cs coverages, 2/16 θ, 4/16 θ, 6/16 θ, and 8/16 θ, respectively. Notice: the adsorption energy at the normal in (c) is zero means the normal structure does not exist after relaxation. The adsorption energy of cesium on clean Mo surface is obtained from our previous results [24].

coverage, and by 0.63 eV for 8/16 θ Cs coverage, respectively. From Eq. (1), the average adsorption energy is the sum of $\Delta E_1/n$, $\Delta E_2/n$, and $\Delta E_3/n$. We can see that the contribution of ΔE_2 to the adsorption energy is insignificant, and ΔE_3 becomes important at high Cs coverage. Compared to ΔE_2 and ΔE_3, it is evident that ΔE_1, which reflects the direct Cs-substrate interactions, plays the most significant role and accounts for most of the Cs adsorption energy. This indicates that bonding on the Cs-substrate is strong and dominant.

In the "tilted" cases (see Fig. 1), increasing the Cu coverage has a limited impact on the formation energy of the Cs layer (ΔE_3), but it significantly enhances the interaction between Cs and the substrate, making Cs more easily bound to the surface. Compared to the low Cs coverage, the average adsorption energy of high Cs coverage decreases. That is because the increase of Cs coverage causes Cs atoms to repel and compete with each other as they interact with the substrate, it is consistent with some previous alkali metal adsorption experiments [46]. For Cs co-deposition with W impurity, the adsorption energy does not always increase with the increase of W coverage. This may be related to the average height of the Cs layer above the Mo substrate. In the following Fig. 6 and Fig. 7, the average height of the Cs layer above the Mo substrate is plotted at different impurity coverages and different cesium coverages. The results indicate that as impurity coverage increases, the average height of the Cs layer also increases. The difference lies in the fact that, with copper impurity coverage, the average height of the Cs layer decreases as the cesium coverage increases, whereas with tungsten impurity coverage, the average height of the Cs layer increases with an increase in cesium coverage. Excessive Cs layer height can weaken the interaction between cesium and the molybdenum substrate. It's worth pointing out that the Cs atoms leave their most stable position from the bridge site to the hollow site when co-deposition with impurities as shown in Fig. 1. This will also affect the average adsorption energy of Cs to some extent. In the "normal" cases (see Fig. 1), it's extremely unstable. The reason is also simple, the impurities push the Cs to a higher position, making the interaction between Cs and Mo further weakened. The later work function calculation and analysis will not consider this situation.

3.2. *Work function*

Deposition of cesium atoms on the surface is one effective way to reduce the work function. This is attributed to the charge transfer between surface atoms and adsorbed atoms, which affects the Fermi level of system. Additional impurity atoms, such as copper and tungsten, also influence the charge distribution on the cesiated surface, thereby affecting the surface work function. Fig. 3 shows the calculation results of the work function of Cs co-deposition with Cu and W metal impurities. The deposition of copper and tungsten on the surface exhibits completely opposite properties. The work function of clean Mo (0 0 1) surface is 4.40 eV.Under conditions without cesium, Deposition of copper increases the surface work function, and as the coverage of copper increases, the work function consistently increases, from 4.56 eV (2/16 θ) to 4.95 eV (8/16 θ). On the other hand, deposition of tungsten reduces the surface work function, and with an increasing coverage of tungsten, the work function consistently decreases from 4.06 eV (2/16 θ) to 3.46 eV (8/16 θ). The work functions of pure cesium (from 2/16 θ to 8/16 θ) deposition are 2.41 eV, 1.70 eV, 1.72 eV, and 1.78 eV, respectively.

Under the conditions co-deposition with cesium, as shown in Fig. 3 (a), at the low Cs coverage, Cu impurity increases the work function. The degree of increase, however, gradually decreases with the increase of Cs coverage. The inversion occurs between the Cs coverage of 4/16 θ and 6/16 θ. At 4/16 θ Cs coverage, the work functions (from 2/16 θ to 8/16 θ Cu coverage) are 1.80 eV, 1.85 eV, 1.86 eV, and 2.02 eV, respectively. The work functions higher than 4/16 θ pure Cs coverage. At 6/16 θ Cs coverage, the work functions are 1.69 eV, 1.70 eV, 1.58 eV, and 1.66 eV, respectively. The work functions lower than 6/16 θ pure Cs coverage.

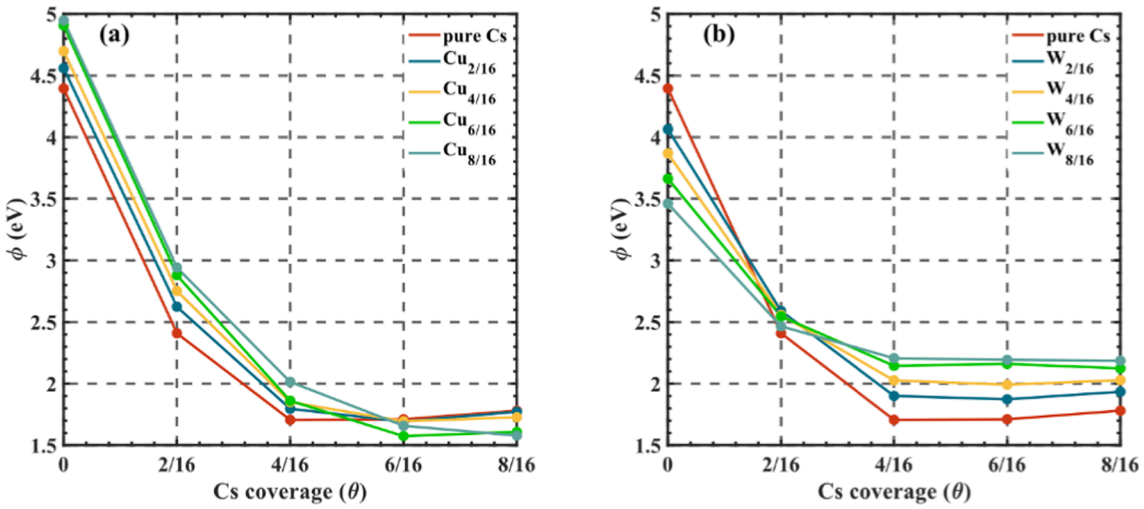

Fig. 3. Work function versus deposition coverage of Cs on: (a) Cu-covered Mo (001); (b) W-covered Mo (001). The work functions of cesium on clean Mo surface is obtained from our previous results [24].

Moreover, the minimum work function corresponds to the Cs coverage of 4/16 θ when pure Cs adsorbs, that is the half monolayers. Although 4/16 θ and 6/16 θ correspond to very close work functions, one can at least assume that the minimum work function corresponds to a coverage range between 4/16 θ and 6/16 θ. The co-adsorption of Cu impurities causes the lowest point of the work function to shift towards higher Cs coverage. This deviation is more obvious with the increase in impurity content. At low Cu coverage, the minimum work function corresponds to the Cs coverage of 6/16 θ. When the coverage of Cu reaches 8/16 θ, the lowest point of work function shifts towards the Cs coverage of 8/16 θ, that is the monolayer. As opposed to Cu impurities, as shown in Fig. 3 (b), the W impurity always increases the work function. At 2/16 θ Cs coverage, the increase caused by W is limited, and the greater the coverage of W, the smaller the increase of work function. But at the two most prominent cesium coverages, 4/16 θ and 8/16 θ (corresponding to 0.5 ML and 1.0 ML, respectively), tungsten deposition has the most noticeable impact on the increase in the work function. Especially at 4/16 θ Cs and 8/16 θ W coverage increases the work function by 0.50 eV, and at 8/16 θ Cs and 8/16 θ W coverage increases the work function by 0.40 eV.

3.3. Dipole moment density induced by electron density difference

Work function is an important parameter that affects the efficiency of negative ion production. Because metal impurities can significantly alter the work function of cesiated surfaces, it is necessary to further analyze and explain the trends in work function variation under conditions of metal impurity deposition. Based on this purpose, the dipole moment densities of different surfaces were calculated and plotted. The change in surface work function is largely determined by the charge transfer and polarization between the substrate and the adsorbed atoms. This charge transfer will change the surface dipole moment density and surface electrical field. Eq. (2) shows the relationship between the change in work function and the change in dipole moment density [47]:

$$\phi - \phi_0 = -180.95(p - p_0)\# \tag{2}$$

where the ϕ and ϕ_0 represent the work function of adatom-covered Mo (001) surface and clean Mo (001) surface, respectively. p and p_0 represent the dipole moment density of the adatom-covered Mo (001) surface and clean Mo (001) surface, respectively. The dipole moment density of the system is calculated as follows:

$$p = \int_0^{z_c} z\rho_z dz\# \tag{3}$$

where the integration is limited to the volume ranging from the bottom of the cell up to the middle of the vacuum layer. ρ_z is the one-dimensional electron density difference obtained by taking the planar average of the three-dimensional charge density difference $\rho(r)$. There is a clear linear relationship between these two parameters, with a slope of −180.95. The slopes of Cs-Cu system and Cs-W system are −183.27 and −186.45 in this work. The results of $p - p_0$ are shown in Fig. 4. One can easily notice that this plot mirrors the changes in work function.

The change in dipole moments is primarily determined by charge transfer and polarization induced by adsorbed atoms. The additional dipole moment density, Δp, normal to the surface caused by this charge redistribution can be calculated by substituting $\Delta\rho_z$ from Eq. (4) into Eq. (3) and replacing the ρ_z integral,

$$\begin{aligned}\Delta\rho_z &= \frac{1}{A}\int_0^a dx \int_0^b dy \Delta\rho(r) \\ &= \frac{1}{A}\int_0^a dx \int_0^b dy \{\rho_{Mo+adatom}(r) - [\rho_{Mo}(r) + \rho_{Cs}(r) + \rho_{imp.}(r)]\}\#\# \\ &\#\end{aligned} \tag{4}$$

where A is the area of the XY-plane of the cell, equals a multiply b. $\rho_{Mo+adatom}(r)$, $\rho_{Mo}(r)$, $\rho_{Cs}(r)$, and $\rho_{imp.}(r)$ are the electron density of the conjugate system, the deformed Mo surface, the Cs layer, and the impurity layer (Cu or W), respectively. As shown in Fig. 5, the overall trend of Δp is consistent with $p - p_0$, and they are also close in numerical value. The difference between the two exists because another factor that can cause changes in the dipole moment is overlooked. That is the impact of surface deformation. Any adsorbed atom can cause deformation of the surface Mo atomic layer, which is also one aspect that leads to the change in dipole moment, contributing to $p - p_0$. However, since the contribution is too small, it will not be discussed in detail here. Under conditions without cesium, the deposition of both copper and tungsten results in an additional dipole moment, which strengthens with increasing coverage. The difference lies in the direction of the additional dipole moment induced by copper, which points towards the surface, while the additional dipole moment induced by tungsten points towards the vacuum. The dipole moment directed towards the surface inhibits electron escape, leading to an increase in the work function. Conversely, the dipole moment directed towards the vacuum assists electron escape, resulting in a decrease in the work function. Under conditions with cesium, as shown in Fig. 5 (a), under a cesium coverage of less than 4/16 θ, the Cu impurity causes the dipole moment density to decrease. Compared to pure cesium deposition, the introduction of copper is

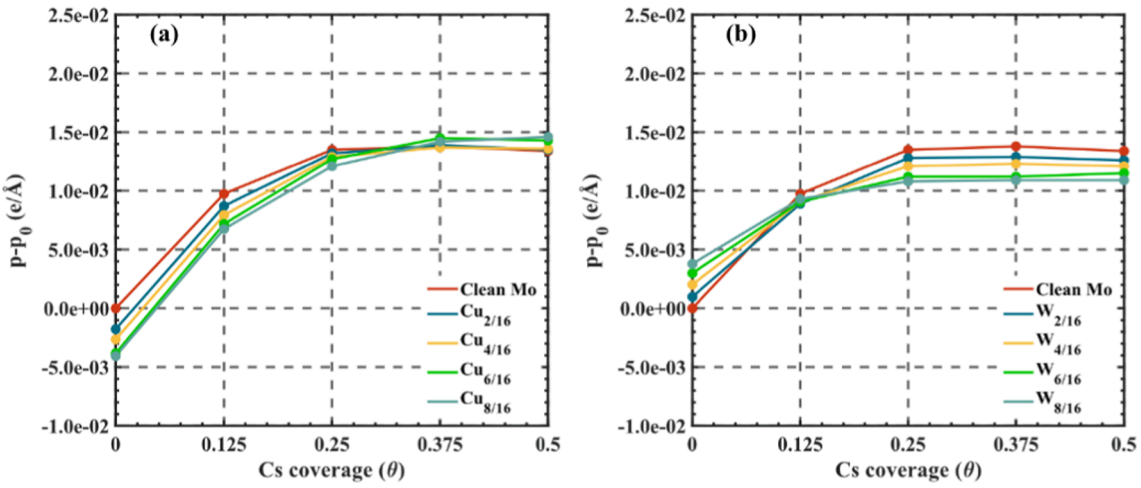

Fig. 4. Surface dipole moment density difference versus deposition coverage of Cs on: (a) Cu-covered Mo (001); (b) W-covered Mo (001). $p - p_0$ of cesium on clean Mo surface is obtained from our previous results [24].

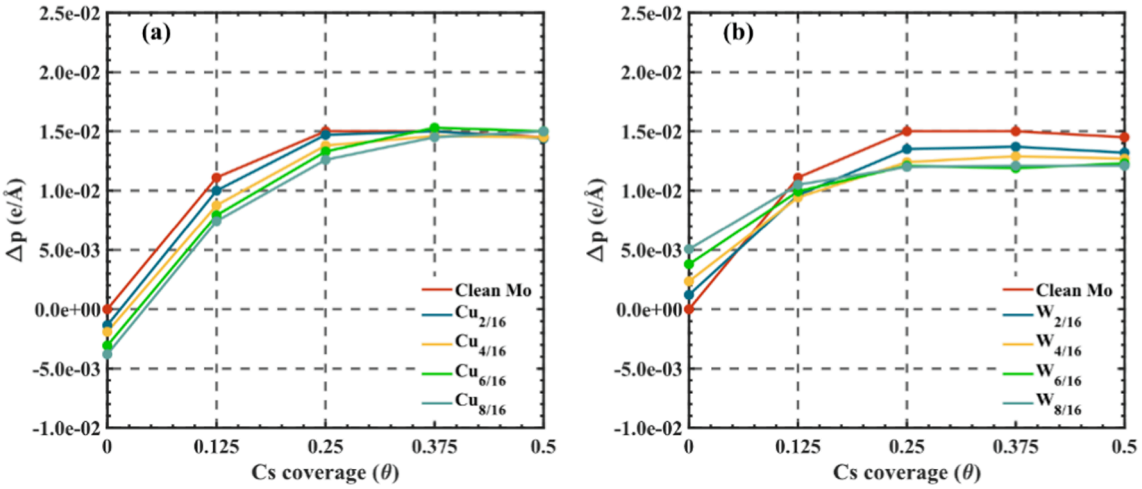

Fig. 5. The dipole moment density, Δp, induced by charge redistribution versus deposition coverage of Cs on: (a) Cu-covered Mo (001); (b) W-covered Mo (001). Δp of cesium on clean Mo surface is obtained from our previous results [24].

equivalent to inducing an additional dipole moment pointing towards the surface, with values of −3.37 E-04 e/Å, −1.29 E-03 e/Å, −1.74 E-03 e/Å, and −2.46 E-03 e/Å, respectively. This is consistent with Eq. (2). As the amount of cesium increases, the impact of the impurity gradually weakens. At a cesium coverage of 8/16 θ, the additional dipole moments induced by cooper are −1.41 E-04 e/Å, 1.04 E-04 e/Å, 4.49 E-04 e/Å, and 4.59 E-04 e/Å, respectively. Low-coverage Cu impurity does not affect the change in dipole moment density, while the high-coverage Cu impurity can increase the dipole moment density. Different from Cu impurity, W impurities can decrease the dipole moment density under any Cs coverage and W coverage. At 4/16 θ Cs, the additional dipole moments induced by tungsten are −1.59 E-03 e/Å, −2.60 E-03 e/Å, −2.99 E-03 e/Å, and −3.01 E-03 e/Å, respectively. At 8/16 θ Cs, the additional dipole moments induced by tungsten are −1.25 E-03 e/Å, −1.82 E-03 e/Å, −2.23 E-03 e/Å, and −2.36 E-03 e/Å, respectively. So the work function of the Cs-W co-adsorbed surface is higher than the work function of the surface with pure cesium adsorption.

3.4. Dipole moment density induced by charge transfer and polarization

Δp represents the results of charge redistribution among the Mo (001) substrate, cesium, and impurities. This includes contributions from both charge transfer and charge polarization. The dipole moment density μ_T caused by charge transfer can be evaluated using the following equation:

$$\mu_T = \sum_i^n q_i r_i / A = \mu_{Mo} + \mu_{imp.} + \mu_{Cs} = \left(\sum_{i_{Mo}}^{n_{Mo}} q_{i_{Mo}} r_{i_{Mo}} + \sum_{i_{imp.}}^{n_{imp.}} q_{i_{imp.}} r_{i_{imp.}} + \sum_{i_{Cs}}^{n_{Cs}} q_{i_{Cs}} r_{i_{Cs}}\right)/A\# \quad (5)$$

where q_i is the Hirshfeld-I [48] charge of the i-th atom in the system, and r_i is the average height of the i-th atom from the topmost Mo layer. It can be observed that the overall variation trends of μ_T and Δp are consistent. However, there is still a certain gap in terms of numerical values. We will discuss this at the end.

It can be clearly seen that μ_T is lower than and mainly determined by μ_{Cs}, as shown in Fig. 6 and Fig. 7. This is because the Cs layer has a higher elevation relative to the surface and a larger positive charge amount. The average height of the impurities from the surface is less than 1.4 Å, while the average height of cesium from the surface is greater than 3.0 Å. At 2/16 θ copper (tungsten) coverage, the charge amounts of the cesium layer are as follows: 0.69 e, 0.97 e, 1.06 e, and 1.13 e (0.63 e, 0.94 e, 1.07 e, and 1.16 e); at 4/16 θ copper (tungsten) coverage, the charge amounts of the cesium layer are as follows: 0.68 e, 0.99 e, 1.11 e, and 1.20 e (0.59 e, 0.89 e, 1.12 e, and 1.23 e); at 6/16 θ copper

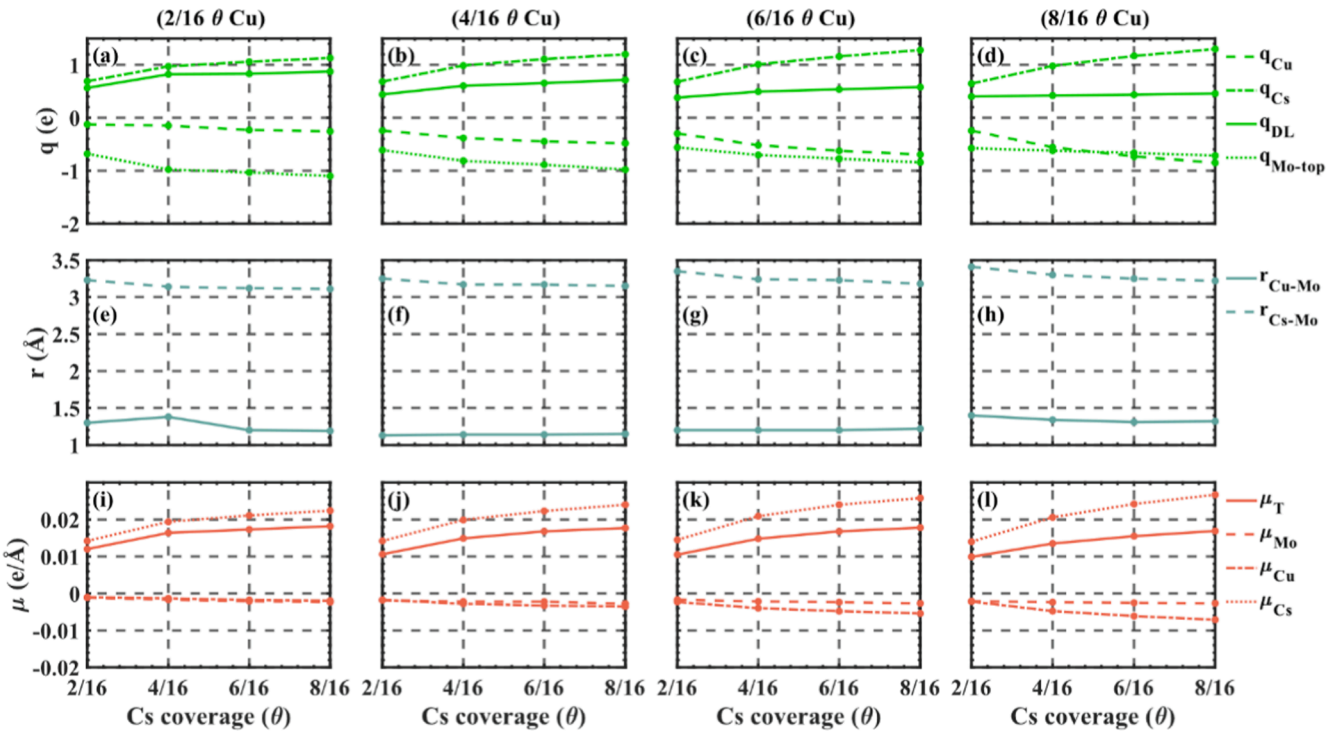

Fig. 6. Under different coverages of Cs and Cu impurities: (a)-(d), the HI charge acquired by the Cu layer, the Cs layer, the Cs-Cu double layer, and the topmost Mo layer, respectively; (e)-(h), the average distance of the Cu layer and Cs layer from the topmost Mo layer respectively; (i)-(l), the dipole moment density caused by the total HI charge transfer of Cs/Cu/Mo system, Mo-substrate charge, Cu layer charge, Cs layer charge, respectively.

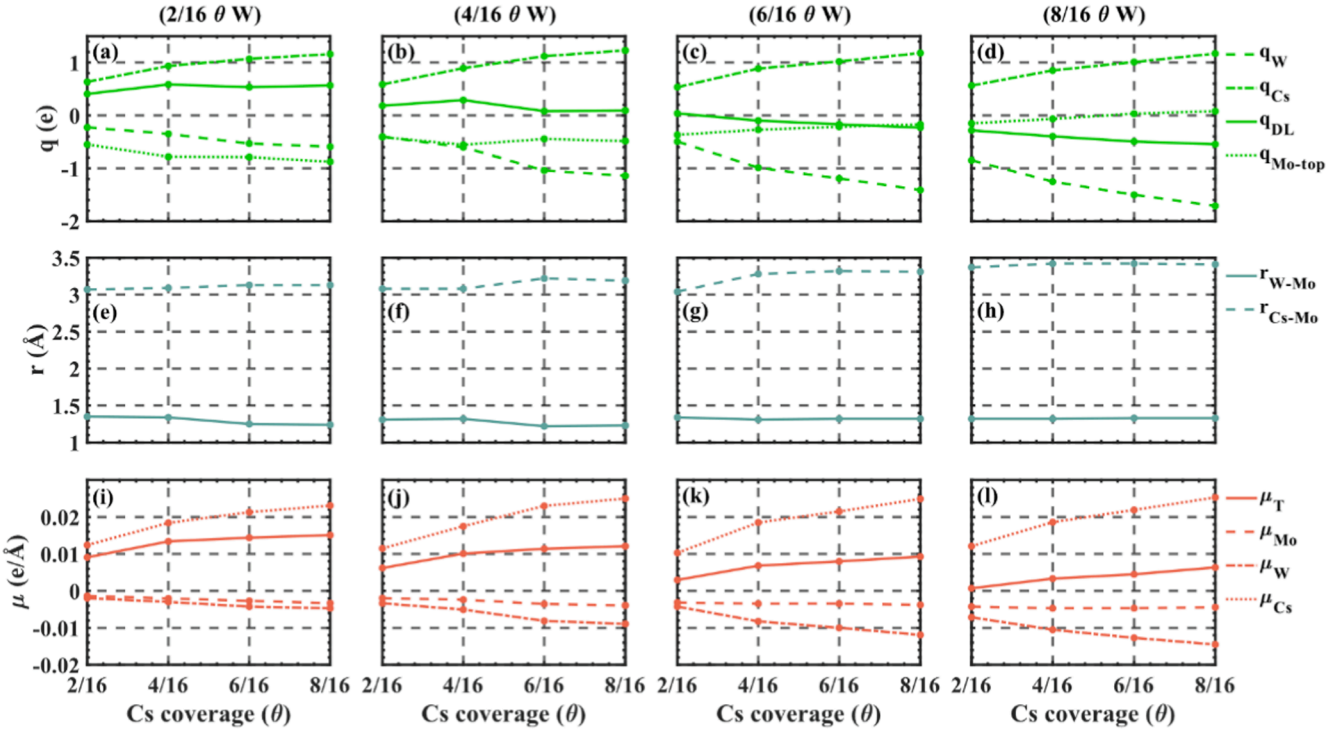

Fig. 7. Under different coverages of Cs and W impurities: (a)-(d), the HI charge acquired by the W layer, the Cs layer, the Cs-W double layer, and the topmost Mo layer, respectively; (e)-(h), the average distance of the W layer and Cs layer from the topmost Mo layer respectively; (i)-(l), the dipole moment density caused by the total HI charge transfer of Cs/W/Mo system, Mo-substrate charge, W layer charge, Cs layer charge, respectively.

(tungsten) coverage, the charge amounts of the cesium layer are as follows: 0.68 e, 1.01 e, 1.16 e, and 1.28 e (0.53 e, 0.87 e, 1.02 e, and 1.18 e); at 8/16 θ copper (tungsten) coverage , the charge amounts of the cesium layer are as follows: 0.65 e, 0.98 e, 1.17 e, and 1.30 e (0.56 e, 0.85 e, 1.01 e, and 1.17 e). The charge of the cesium layer increases with the increase in cesium coverage. However, the slope significantly

decreases, indicating a gradual reduction in the average charge of cesium atoms. The decrease in the average charge suggests that with increasing cesium coverage, cesium atoms transition gradually from ionic to metal properties, ultimately aligning with the characteristics of cesium metal. This is consistent with the previous findings reported by Said et al. [33].

Under the co-adsorption conditions with Cu, the charge amount of the Cs layer increases with the increase of Cu coverage. However, the effect of W coverage on the charge amount of the Cs layer is not significant. Given that the charge amount of the Cs layer is a key factor influencing dipole moment density and consequently the work function, a Cs layer with a larger charge is beneficial for reducing the work function. Furthermore, compared to the W impurity condition, the height of cesium under the Cu impurity condition is lower, which would result in a decreased dipole moment density.

In summary, μ_{Cs} under the Cu impurity condition is slightly larger. However, Another key factor is the charge amount in the impurity layer. As shown in Figs. 6 and 7, at 2/16 θ impurity coverage, the charge amounts of the copper (tungsten) layer greater than −0.26 e (-0.59 e); at 4/16 θ impurity coverage, the charge amounts of the copper (tungsten) layer greater than −0.48 e (-1.14 e); at 6/16 θ impurity coverage, the charge amounts of the copper (tungsten) layer greater than −0.70 e (-1.41 e); at 8/16 θ impurity coverage, the charge amounts of the copper (tungsten) layer greater than −0.85 e (-1.71 e). This is evident that the negative charge amount in the W impurity layer is greater. Regardless of whether it's Cu or W, the heights of the impurities are similar. Therefore, μ_W is much smaller than μ_{Cu}. Taken together, the amount of charge in the impurity layer plays a dominant role in influencing the final dipole moment. This explains the higher dipole moment density observed under Cu impurity conditions compared to W impurity conditions in Fig. 5. The deposition of cesium and impurities on the surface forms a double layer structure, and the total charge of this double layer structure, μ_{DL}, is shown in Figs. 6 and 7. It can be seen that μ_{DL} is greater than zero, and the extra charge of the double-layer structure comes from the Mo (0 0 1) substrate. To understand the charge distribution of each Mo layer in the Mo substrate, the charge of the topmost Mo layer, μ_{Mo}, was specifically calculated. It is evident that the charge of the topmost Mo layer plus the total charge of the double layer is less than zero. This implies that electrons in the bulk migrate to the surface under the influence of the adsorbate, and the molybdenum atom in the bulk phase as a whole has an additional positive charge, and because the distance from the surface to this part of the atom is negative. Therefore, μ_{Mo} is always less than zero, which reduces the overall surface dipole moment density.

The dipole moment density caused by charge transfer, μ_T, is only a part of Δp. The other part is the change in dipole moment density, μ_p, caused by charge polarization [49], which can only be estimated by subtracting μ_T from Δp (not plotted here). The results show that under Cu impurity conditions, μ_p is always less than zero, and its impact on Δp is minimal. This suggests that a small portion of the charge in the Cs/Cu/Mo system always polarizes downward. For the W impurity conditions, μ_p has a minimal effect on Δp at 2/16 θ W impurity coverage and becomes slightly more noticeable at 8/16 θ Cs coverage and it's also less than zero. As W coverage increases, the impact of μ_p becomes more pronounced, dominating at 8/16 θ W coverage. Moreover, under high W coverage, μ_p is always greater than zero, indicating that some of the charge in the system always polarizes upward. Additionally, under W impurity coverage, μ_p consistently decreases with increasing Cs coverage, a trend consistent with μ_p changes under pure Cs adsorption conditions.

4. Conclusions

In this study, The effect of metal impurities, including copper and tungsten, on the average adsorption energy of Cs atoms on Mo (0 0 1) surface and the work function of cesiated surface has been studied at the DFT level.

Firstly, the average adsorption energy of cesium on the surface was evaluated. The results indicate that copper impurities significantly enhance the average adsorption energy of cesium, while tungsten has a limited effect on it, in some coverages, can even decrease it. One of the reasons for this is that when co-adsorbed with tungsten, the equilibrium height of the cesium layer above the substrate is higher. Secondly, the calculated results of the work function reveal that copper impurities exhibit a significant enhancement in the work function at low cesium coverages, but the effect diminishes at high cesium coverages. With increasing copper coverage, the cesium coverage corresponding to the minimum work function shifts towards higher coverages. In contrast, tungsten impurities significantly increase the work function of cesium-covered surfaces under all conditions. Thirdly, the changes in the work function have been analyzed and explained by the surface dipole moment density. The change in work function shows a linear relationship with the variation in surface dipole moment density. The deposition of cesium and impurity atoms generates additional dipole moments, where negative dipole moments point towards the vacuum, resulting in a decrease in the work function, while negative dipole moments pointing towards the surface increase the work function. Only at a 2/16 θ impurity coverage, the additional negative dipole moment induced by copper deposition on cesiated surface is larger. The formation of additional dipole moments is primarily determined by charge redistribution, including charge transfer (μ_T) and charge polarization (μ_p). Compared to with tungsten, the depositon of cooper induces a larger charge amount of cesium layer, a smaller negative charge of impurity layer, and a stronger negative dipole moment induced by polarization.

The main objective of this study is to understand the influence of copper and tungsten metal impurities on cesiated surfaces at different coverages, including the average adsorption energy and surface work function of cesium. Hydrogen isotopes were not considered due to the complexity it introduces in terms of surface structures and computational demands. In future work, the introduction of hydrogen isotopes will be considered at specific coverages, and statistical analysis will be conducted.

CRediT authorship contribution statement

Heng Li: Writing – original draft, Visualization, Methodology, Investigation, Formal analysis, Data curation, Conceptualization. **Xin Zhang:** Validation, Supervision, Software, Resources, Funding acquisition. **Yuhong Xu:** Validation, Supervision, Software, Resources, Project administration, Funding acquisition. **Guangjiu Lei:** Validation, Supervision, Funding acquisition. **Sanqiu Liu:** Validation, Resources, Funding acquisition. **Katsuyoshi Tsumori:** Validation, Supervision, Resources, Funding acquisition. **Haruhisa Nakano:** Validation, Resources. **Masaki Osakabe:** Validation, Resources. **Mitsutaka Isobe:** Validation, Supervision, Resources. **Shoichi Okamura:** Validation, Supervision, Resources. **Akihiro Shimizu:** Validation, Resources. **Kunihiro Ogawa:** Validation, Resources. **Hiromi Takahashi:** Validation, Resources. **Zilin Cui:** Visualization, Validation, Software. **Jun Hu:** Validation, Resources, Methodology. **Yiqin Zhu:** Validation. **Xiaolong Li:** Validation. **Huaqing Zheng:** Validation. **Xiaoqiao Liu:** Validation, Software. **Shaofei Geng:** Validation, Supervision, Methodology. **Xiaochang Chen:** Validation, Funding acquisition. **Haifeng Liu:** Validation, Resources. **Xianqu Wang:** Validation, Supervision, Resources. **Hai Liu:** Validation. **Changjian Tang:** Validation, Supervision.

Declaration of competing interest

The authors declare that they have no known competing financial interests or personal relationships that could have appeared to influence the work reported in this paper.

Data availability

Data will be made available on request.

Acknowledgments

This work was supported by the Natural Science Foundation of Sichuan Province (No.2022NSFSC0331), Sichuan International Science and Technology Innovation Cooperation Project (2021YFH0066), National Key R&D Program of China (2022YFE03070000: 2022YFE03070002). This work was also supported by the NIFS general collaboration project, NIFS18KBAP041, NIFS19KLPP057, NIFS20KBAP067,NIFS22KIPH009, NIFS22KIPH010, NIFS22KIPH011, NIFS22KIEE001, and "PLADyS", JSPS Core-to-Core Program, A. Advanced Research Networks. The work was carried out at National Supercomputer Center in Tianjin, and this research was supported by TianHe Qingsuo Project special fund project.

References

[1] U. Fantz, P. Franzen, D. Wünderlich, Development of negative hydrogen ion sources for fusion: Experiments and modelling, Chem. Phys. 398 (2012) 7–16, https://doi.org/10.1016/j.chemphys.2011.05.006.
[2] R.S. Hemsworth, T. Inoue, Positive and negative ion sources for magnetic fusion, IEEE Trans. Plasma Sci. 33 (2005) 1799–1813, https://doi.org/10.1109/TPS.2005.860090.
[3] M. Bacal, M. Wada, Negative hydrogen ion production mechanisms, Appl. Phys. Rev. 2 (2015) 021305, https://doi.org/10.1063/1.4921298.
[4] M. Taniguchi, T. Inoue, M. Kashiwagi, K. Watanabe, M. Hanada, T. Seki, M. Dairaku, K. Sakamoto, Acceleration of MeV-class energy, high-current-density H−-ion beams for ITER neutral beam system, Rev. Sci. Instrum. 77 (2006) 03A514, https://doi.org/10.1063/1.2165748.
[5] M. Boldrin, M. Simon, G. Escudero Gomez, M. Krohn, H. Decamps, T. Bonicelli, V. Toigo, The High Voltage Deck 1 and Bushing for the ITER Neutral Beam Injector: Integrated design and installation in MITICA experiment, Fusion Eng. Design 146 (2019) 1895–1898, https://doi.org/10.1016/j.fusengdes.2019.03.059.
[6] W. Kraus, D. Wünderlich, U. Fantz, B. Heinemann, F. Bonomo, R. Riedl, Deuterium results at the negative ion source test facility ELISE, Rev. Sci. Instrum. 89 (2018) 052102, https://doi.org/10.1063/1.5012591.
[7] G. Chitarin, G. Serianni, V. Toigo, M. Bigi, M. Boldrin, S.D. Bello, L. Grando, A. Luchetta, D. Marcuzzi, R. Pasqualotto, N. Pomaro, P. Zaccaria, L. Zanotto, P. Agostinetti, M. Agostini, V. Antoni, D. Aprile, M. Barbisan, M. Battistella, M. Brombin, R. Cavazzana, M.D. Palma, M. Dan, A. De Lorenzi, R. Delogu, M. De Muri, S. Denizeau, M. Fadone, F. Fellin, L. Ferbel, A. Ferro, E. Gaio, G. Gambetta, F. Gasparini, F. Gnesotto, P. Jain, A. Maistrello, G. Manduchi, S. Manfrin, G. Marchiori, N. Marconato, M. Moresco, T. Patton, M. Pavei, S. Peruzzo, N. Pilan, A. Pimazzoni, R. Piovan, C. Poggi, M. Recchia, A. Rizzolo, G. Rostagni, E. Sartori, M. Siragusa, P. Sonato, S. Spagnolo, M. Spolaore, C. Taliercio, P. Tinti, M. Ugoletti, M. Valente, A. Zamengo, B. Zaniol, M. Zaupa, C. Baltador, M. Cavenago, D. Boilson, C. Rotti, P. Veltri, T. Bonicelli, A. Chakraborty, H. Patel, N.P. Singh, U. Fantz, B. Heinemann, W. Kraus, Start of SPIDER operation towards ITER neutral beams, in: Novosibirsk, Russia, 2018, p. 030001. https://doi.org/10.1063/1.5083729.
[8] V. Toigo, S. Dal Bello, M. Bigi, M. Boldrin, G. Chitarin, L. Grando, A. Luchetta, D. Marcuzzi, R. Pasqualotto, N. Pomaro, G. Serianni, P. Zaccaria, L. Zanotto, P. Agostinetti, M. Agostini, V. Antoni, D. Aprile, M. Barbisan, M. Battistella, M. Brombin, R. Cavazzana, M. Dalla Palma, M. Dan, S. Denizeau, A. De Lorenzi, R. Delogu, M. De Muri, M. Fadone, F. Fellin, A. Ferro, A. Fiorentin, E. Gaio, G. Gambetta, F. Gasparini, F. Gnesotto, P. Jain, A. Maistrello, G. Manduchi, S. Manfrin, G. Marchiori, N. Marconato, M. Moresco, E. Ocello, T. Patton, M. Pavei, S. Peruzzo, N. Pilan, A. Pimazzoni, R. Piovan, C. Poggi, M. Recchia, A. Rizzolo, G. Rostagni, E. Sartori, M. Siragusa, P. Sonato, A. Sottocornola, E. Spada, S. Spagnolo, M. Spolaore, C. Taliercio, P. Tinti, M. Ugoletti, M. Valente, A. Zamengo, B. Zaniol, M. Zaupa, D. Boilson, C. Rotti, P. Veltri, J. Chareyre, H. Decamps, M. Dremel, J. Graceffa, F. Geli, B. Schunke, L. Svensson, M. Urbani, T. Bonicelli, G. Agarici, A. Garbuglia, A. Masiello, F. Paolucci, M. Simon, L. Bailly-Maitre, E. Bragulat, G. Gomez, D. Gutierrez, C. Labate, G. Mico, J.F. Moreno, V. Pilard, G. Kouzmenko, A. Rousseau, M. Kashiwagi, H. Tobari, K. Watanabe, T. Maejima, A. Kojima, N. Umeda, S. Sasaki, A. Chakraborty, U. Baruah, H. Patel, N.P. Singh, A. Patel, H. Dhola, B. Raval, V. Gupta, U. Fantz, B. Heinemann, W. Kraus, M. Cavenago, S. Hanke, S. Ochoa, P. Blatchford, B. Chuilon, Y. Xue, G. Croci, G. Gorini, A. Muraro, M. Rebai, M. Tardocchi, M. D'Arienzo, S. Sandri, A. Tonti, F. Panin, Progress in the ITER neutral beam test facility, Nucl. Fusion 59 (2019) 086058, https://doi.org/10.1088/1741-4326/ab2271.
[9] U. Fantz, P. Franzen, B. Heinemann, D. Wünderlich, First results of the ITER-relevant negative ion beam test facility ELISE (invited), Rev. Sci. Instrum. 85 (2014) 02B305, https://doi.org/10.1063/1.4825386.
[10] K. Ikeda, K. Tsumori, K. Nagaoka, H. Nakano, M. Kisaki, Y. Fujiwara, S. Kamio, Y. Haba, S. Masaki, M. Osakabe, Extension of high power deuterium operation of negative ion based neutral beam injector in the large helical device, Rev. Sci. Instrum. 90 (2019) 113322, https://doi.org/10.1063/1.5128529.
[11] P. Franzen, H.D. Falter, E. Speth, W. Kraus, M. Bandyopadhyay, A. Encheva, U. Fantz, T.h. Franke, B. Heinemann, D. Holtum, C. Martens, P. McNeely, R. Riedl, A. Tanga, R. Wilhelm, Status and plans for the development of a RF negative ion source for ITER NBI, Fusion Eng. Des. 74 (2005) 351–357, https://doi.org/10.1016/j.fusengdes.2005.06.178.
[12] S. Geng, K. Tsumori, H. Nakano, M. Kisaki, K. Ikeda, M. Osakabe, K. Nagaoka, Y. Takeiri, M. Shibuya, Response of H− ions to extraction field in a negative hydrogen ion source, Fusion Eng. Des. 123 (2017) 481–484, https://doi.org/10.1016/j.fusengdes.2017.02.041.
[13] W.M. Haynes, CRC Handbook of Chemistry and Physics, 97th ed., CRC Press, Boca Raton, 2016.
[14] H. Li, X. Zhang, Y. Xu, G. Lei, K. Tsumori, M. Isobe, A. Shimizu, Z. Cui, Y. Zhu, J. Hu, Y. Ni, S. Geng, H. Liu, X. Wang, J. Huang, H. Liu, J. Cheng, C. Tang, C. Team, Theoretical calculation of cesium deposition and co-deposition with electronegative elements on the plasma grid in negative ion sources, Nucl. Mater. Energy 34 (2023) 101334, https://doi.org/10.1016/j.nme.2022.101334.
[15] C.A. Papageorgopoulos, J.M. Chen, Coadsorption of electropositive and electronegative elements: I. Cs and H2 on W(100), Sur. Sci. 39 (1973) 283–312, https://doi.org/10.1016/0039-6028(73)90003-4.
[16] C.A. Papageorgopoulos, J.M. Chen, Coadsorption of electropositive and electronegative elements: II. Cs and O2 on W (100), Sur. Sci. 39 (1973) 313–332, https://doi.org/10.1016/0039-6028(73)90004-6.
[17] M. Rutigliano, A. Palma, N. Sanna, Hydrogen scattering from a cesiated surface model, Surf. Sci. 664 (2017) 194–200, https://doi.org/10.1016/j.susc.2017.06.014.
[18] P. Bharathi, A.J. Deka, M. Bandyopadhyay, M. Bhuyan, K. Pandya, R.K. Yadav, H. Tyagi, A. Gahlaut, A. Chakraborty, Study on production and extraction of negative impurity ions in a caesiated negative ion source, Nucl. Fusion 60 (2020) 046008, https://doi.org/10.1088/1741-4326/ab6308.
[19] R. Friedl, U. Fantz, Influence of H_2 and D_2 plasmas on the work function of caesiated materials, J. Appl. Phys. 122 (2017) 083304, https://doi.org/10.1063/1.5000373.
[20] A. Palma, N. Sanna, M. Rutigliano, Evidence of superoxide-like CsO2 formation on a cesiated model surface, Appl. Surf. Sci. 534 (2020) 147579, https://doi.org/10.1016/j.apsusc.2020.147579.
[21] H. Said, T. Bučko, Effect of molecular impurities on properties of clean and cesiated Mo(001) surface: A DFT study of the low coverage limit, Appl. Surf. Sci. 605 (2022) 154706, https://doi.org/10.1016/j.apsusc.2022.154706.
[22] L. Schiesko, C. Hopf, P. Franzen, W. Kraus, R. Riedl, U. Fantz, A study on backstreaming positive ions on a high power negative ion source for fusion, Nucl. Fusion 51 (2011) 113021, https://doi.org/10.1088/0029-5515/51/11/113021.
[23] R. Gutser, C. Wimmer, U. Fantz, Work function measurements during plasma exposition at conditions relevant in negative ion sources for the ITER neutral beam injection, Rev. Sci. Instrum. 82 (2011) 023506, https://doi.org/10.1063/1.3541790.
[24] H. Li, X. Zhang, Y. Xu, G. Lei, S. Liu, K. Tsumori, H. Nakano, M. Osakabe, M. Isobe, S. Okamura, A. Shimizu, K. Ogawa, H. Takahashi, Z. Cui, J. Hu, Y. Zhu, X. Li, H. Zheng, X. Liu, S. Geng, X. Chen, H. Liu, X. Wang, H. Liu, C. Tang, C. Team, Effect of H atoms and O impurities on the adsorption stability and work function of the cesiated Mo(0 0 1) surface: A study about negative hydrogen ion sources for neutral beam injection systems, Nuclear Materials and Energy 37 (2023) 101550, https://doi.org/10.1016/j.nme.2023.101550.
[25] A. Abraham, B. Padama, W. Agerico Diño, M. Wada, K. Tsumori, M. Kisaki, H. Kasai, H. Nakanishi, M. Sasao, N. Tanaka, Adsorption of H on Cs/W(110): Impact of H on the Stability of Cs on the Surface, E-JSSNT 16 (2018) 391–395, https://doi.org/10.1380/ejssnt.2018.391.
[26] W. Kraus, M. Berger, U. Fantz, P. Franzen, M. Fröschle, B. Heinemann, R. Riedl, E. Speth, A. Stäbler, D. Wünderlich, E. Surrey, A. Simonin, Long Pulse H[sup −] Beam Extraction With A RF Driven Ion Source With Low Fraction Of Co-Extracted Electrons, in: AIP Conference Proceedings, AIP, Aix-en-Provence (France), 2009, pp. 275–281. https://doi.org/10.1063/1.3112522.
[27] Y. Takeiri, Negative ion source development for fusion application (invited)a), Rev. Sci. Instrum. (2014).
[28] U. Fantz, P. Franzen, W. Kraus, M. Berger, S. Christ-Koch, H. Falter, M. Fröschle, R. Gutser, B. Heinemann, C. Martens, P. McNeely, R. Riedl, E. Speth, A. Stäbler, D. Wünderlich, Physical performance analysis and progress of the development of the negative ion RF source for the ITER NBI system, Nucl. Fusion 49 (2009) 125007, https://doi.org/10.1088/0029-5515/49/12/125007.
[29] W. Kraus, U. Fantz, P. Franzen, M. Fröschle, B. Heinemann, R. Riedl, D. Wünderlich, The development of the radio frequency driven negative ion source for neutral beam injectors (invited), Rev. Sci. Instrum. 83 (2012) 02B104, https://doi.org/10.1063/1.3662957.
[30] M. Bandyopadhyay, A.J. Deka, D. Mukhopadhyay, P. Singh, D. Borah, A. Pandey, H. Tyagi, R.K. Yadav, M. Bhuyan, P. Bharathi, A.K. Chattopadhyay, K. Pandya, M. J. Singh, A. Chakraborty, Performance evaluation of various diagnostics developed for a negative ion based neutral beam injector program in IPR, Nucl. Fusion 59 (2019) 085001, https://doi.org/10.1088/1741-4326/ab19e2.
[31] T. Inoue, Y. Matsuda, Y. Ohara, Y. Okumura, M. Bacal, P. Berlemont, Effect of filament material and area on the extracted current from a volume H ¯ ion source, Plasma Sources Sci. Technol. 1 (1992) 75–81, https://doi.org/10.1088/0963-0252/1/2/001.
[32] Y. Takeiri, O. Kaneko, K. Tsumori, Y. Oka, K. Ikeda, M. Osakabe, K. Nagaoka, E. Asano, T. Kondo, M. Sato, M. Shibuya, High-power and long-pulse injection with negative-ion-based neutral beam injectors in the Large Helical Device, Nucl. Fusion 46 (2006) S199–S210, https://doi.org/10.1088/0029-5515/46/6/S01.

[33] H. Said, M. Novotný, I. Černušák, T. Bučko, Ab initio molecular dynamics investigation of Cs adsorption on Mo(0 0 1): Beyond a single monolayer coverage, Appl. Surf. Sci. 559 (2021) 149822, https://doi.org/10.1016/j.apsusc.2021.149822.
[34] G. Kresse, J. Furthmüller, Efficient iterative schemes for *ab initio* total-energy calculations using a plane-wave basis set, Phys. Rev. B 54 (1996) 11169–11186, https://doi.org/10.1103/PhysRevB.54.11169.
[35] G. Kresse, Ab initio molecular dynamics for liquid metals, J. Non-Crystalline Solids 192 & 193 (1995) 222–229, https://doi.org/10.1016/0022-3093(95)00355-X.
[36] T.D. Kühne, M. Iannuzzi, M. Del Ben, V.V. Rybkin, P. Seewald, F. Stein, T. Laino, R. Z. Khaliullin, O. Schütt, F. Schiffmann, D. Golze, J. Wilhelm, S. Chulkov, M. H. Bani-Hashemian, V. Weber, U. Borštnik, M. Taillefumier, A.S. Jakobovits, A. Lazzaro, H. Pabst, T. Müller, R. Schade, M. Guidon, S. Andermatt, N. Holmberg, G.K. Schenter, A. Hehn, A. Bussy, F. Belleflamme, G. Tabacchi, A. Glöß, M. Lass, I. Bethune, C.J. Mundy, C. Plessl, M. Watkins, J. VandeVondele, M. Krack, J. Hutter, CP2K: An electronic structure and molecular dynamics software package - Quickstep: Efficient and accurate electronic structure calculations, J. Chem. Phys. 152 (2020) 194103, https://doi.org/10.1063/5.0007045.
[37] P.E. Blöchl, Projector augmented-wave method, Phys. Rev. B 50 (1994) 17953–17979, https://doi.org/10.1103/PhysRevB.50.17953.
[38] J.P. Perdew, K. Burke, M. Ernzerhof, Generalized Gradient Approximation Made Simple, Phys. Rev. Lett. 77 (1996) 3865–3868, https://doi.org/10.1103/PhysRevLett.77.3865.
[39] P. Hohenberg, W. Kohn, Inhomogeneous Electron Gas, Phys. Rev. 136 (1964) B864–B871, https://doi.org/10.1103/PhysRev.136.B864.
[40] S. Grimme, J. Antony, S. Ehrlich, H. Krieg, A consistent and accurate ab initio parametrization of density functional dispersion correction (DFT-D) for the 94 elements H-Pu, J. Chem. Phys. 132 (2010) 154104, https://doi.org/10.1063/1.3382344.
[41] L. Bengtsson, Dipole correction for surface supercell calculations, Phys. Rev. B 59 (1999) 12301–12304, https://doi.org/10.1103/PhysRevB.59.12301.
[42] J. VandeVondele, J. Hutter, Gaussian basis sets for accurate calculations on molecular systems in gas and condensed phases, J. Chem. Phys. 127 (2007) 114105, https://doi.org/10.1063/1.2770708.
[43] S. Goedecker, M. Teter, J. Hutter, Separable dual-space Gaussian pseudopotentials, Phys. Rev. B 54 (1996) 1703–1710, https://doi.org/10.1103/PhysRevB.54.1703.
[44] C. Hartwigsen, S. Goedecker, J. Hutter, Relativistic separable dual-space Gaussian pseudopotentials from H to Rn, Phys. Rev. B 58 (1998) 3641–3662, https://doi.org/10.1103/PhysRevB.58.3641.
[45] D.J. Chadi, Special points for Brillouin-zone integrations, Phys. Rev. B 16 (1977) 1746–1747, https://doi.org/10.1103/PhysRevB.16.1746.
[46] P. Soukiassian, R. Riwan, J. Lecante, E. Wimmer, S.R. Chubb, A.J. Freeman, Adsorbate-induced shifts of electronic surface states: Cs on the (100) faces of tungsten, molybdenum, and tantalum, Phys. Rev. B 31 (1985) 4911–4923, https://doi.org/10.1103/PhysRevB.31.4911.
[47] T.C. Leung, C.L. Kao, W.S. Su, Y.J. Feng, C.T. Chan, Relationship between surface dipole, work function and charge transfer: Some exceptions to an established rule, Phys. Rev. B 68 (2003) 195408, https://doi.org/10.1103/PhysRevB.68.195408.
[48] P. Bultinck, C. Van Alsenoy, P.W. Ayers, R. Carbó-Dorca, Critical analysis and extension of the Hirshfeld atoms in molecules, J. Chem. Phys. 126 (2007) 144111, https://doi.org/10.1063/1.2715563.
[49] T. Roman, A. Groß, Periodic Density-Functional Calculations on Work-Function Change Induced by Adsorption of Halogens on Cu(111), Phys. Rev. Lett. 110 (2013) 156804, https://doi.org/10.1103/PhysRevLett.110.156804.